Asian Journal of Chemistry; Vol. 30, No. 12 (2018), 2754-2760

ASIAN JOURNAL OF CHEMISTRY

https://doi.org/10.14233/ajchem.2018.21615

Synthesis and Characterization of Iron Tartrate Nanoparticles

U.M. LATHIYA[1,*], P.M. VYAS[2], H.O. JETHVA[1], M.J. JOSHI[1] and GIRISH M. JOSHI[3]

[1]Crystal Growth Laboratory, Department of Physics, Saurashtra University, Rajkot-360 005, India
[2]Department of Physics, Kamani Science & Prataprai Arts College, Amreli-365 601, India
[3]Polymer Nanocomposite Lab, Materials Physics Division, School of Advance Sciences, VIT University, Vellore-632 014, India

*Corresponding author: E-mail: urvi.tarpara@gmail.com

Received: 27 July 2018; *Accepted*: 24 September 2018; *Published online*: 31 October 2018; AJC-19143

Considering various applications of iron tartrate, this article aims to synthesize iron tartrate nanoparticles by wet chemical technique using iron(II) sulphate, tartaric acid, sodium metasilicate and surfactant Triton X-100. The presence of sodium metasilicate facilitates the reaction between iron(II) sulphate and tartaric acid to form iron tartrate. The powder XRD study indicates orthorhombic structure and the average crystallite size is found to be 35.28 nm by employing Scherrer's formula. The TEM images indicate nearly spherical morphology with size varying from 30 to 50 nm. The thermal analysis suggests that the nano-particles are stable up to 100 ºC and then decomposes through various stages. The dielectric study is carried out on pelletized samples in the range from 10 Hz to 10 MHz at various temperatures from 303 to 373 K. The dielectric constant and dielectric loss decreases with frequency increases. The a.c. conductivity increased with increasing frequency. The Jonscher's power law is studied for a.c. conductivity and correlated barrier hopping model mechanism is found to be prevailing for a.c. conduction. The activation energy for electrical conduction is decreasing with increasing frequency. The temperature dependent magnetization measurements under zero field cooled (ZFC) and field cooled (FC) condition has indicated the paramagnetic nature of the sample at room temperature as well as low temperature. The results are compared with the bulk crystalline material available in the literature.

Keywords: Iron tartrate nanoparticles, Powder XRD, Dielectric Properties, Vibrating sample magnetometry.

INTRODUCTION

Iron tartrate deserves special attention due to its industrial, biological and pharmaceutical applications; for example, in tanning industry due to oxidizing power Fe(III) and Fe(II) tartrates are used [1], iron being an essential micro-nutrient for plant tissue culture media, a ferric tartrate salt is used in media as iron source [2], caliphylatic response of ferrous tartrate compound to prevent anaemia in animals [3], iron tartrate as a potential precursor of light induced oxidative degradation of white wine [4] and impact of fluorescent lighting on oxidation of wine solutions containing iron [5].

Joshi *et al.* [6,7] have reported the characterizations of iron tartrate crystals grown by the gel method along with mixed iron-manganese tartrate [8] and ternary iron-manganese-cobalt tartrate [9] crystals grown *via* gel method. The literature survey could not find any significant report on iron(II) tartrate nanoparticles synthesis and characterizations. Therefore, the study aim to synthesize iron(II) tartrate nanoparticles by the wet chemical technique and characterize thoroughly by techniques such as powder XRD, TEM, FTIR, TGA, dielectric and magnetic studies.

EXPERIMENTAL

All the AR grade chemicals were used to synthesize the samples. The powder XRD was carried out using Bruker Kappa Apex II X-ray Diffractometer (CCD 4) set up with CuK_α radiation. The data were analyzed with help of software Powder X. The TEM images were recorded on Philips CM 200 (SAIF, IIT Bombay) with extra high tension of 200 kV. The FTIR spectrum was recorded on powdered samples in KBr medium using Nicolet 6700 in the range from 4000 to 400 cm^{-1}. The thermal study was conducted on METTLER TOLEDO TGA/SDTA 851 in atmosphere of nitrogen at heating rate of 15 ºC/min from room temperature to 800 ºC. The magnetic susceptibility

of the nanoparticles was measured using Lakeshore, USA, Model 7407 Vibrating Sample Magnetometer (Department of Chemistry, IIT Madras, Chennai, India) at room temperature and low temperature with different applied magnetic fields.

Synthesis: Iron tartrate nanoparticles were synthesized by wet chemical method and adopting surfactant mediated approach [10]. Aqueous solutions of 1 M iron sulphate, triton X-100, 1 M tartaric acid and 1.05 specific gravity of sodium meta silicate solutions were mixed in appropriate manner with constant stirring by maintaining proper water to surfactant ratio and the pH range from 4 to 5. The reaction did not take place between ferrous sulphate and tartaric acid to form iron(II) tartrate. The sodium meta silicate solution facilitated the reaction to form iron(II) tartrate [10]. It is important to note that sodium meta silicate did not form any product. The resulting precipitates were filtered, washed with deionized water and air dried. The chemical reaction that occurred during the synthesis of iron tartrate nanoparticles is:

$$FeSO_4 + H_2C_4H_4O_6 \longrightarrow FeC_4H_4O_6 + H_2SO_4$$

RESULTS AND DISCUSSION

Powder X-ray diffraction: Fig. 1 indicates the powder X-ray diffraction pattern of iron(II) tartrate nanoparticles. The unit cell parameters (Table-1) were obtained by computer software Powder-X and compared with the bulk material [8]. The average crystallite size was calculated by employing Scherrer's formula and Williamson & Hall equation to powder XRD results. The standard formulations were applied as given by Solanki *et al.* [11]. Table-2 gives the values of average crystallite size and strain. The average crystallite size calculated from Williamson & Hall relation is less than that calculated from Scherrer's formula due to the strain correction factor considered in the Williamson & Hall equation [11,12].

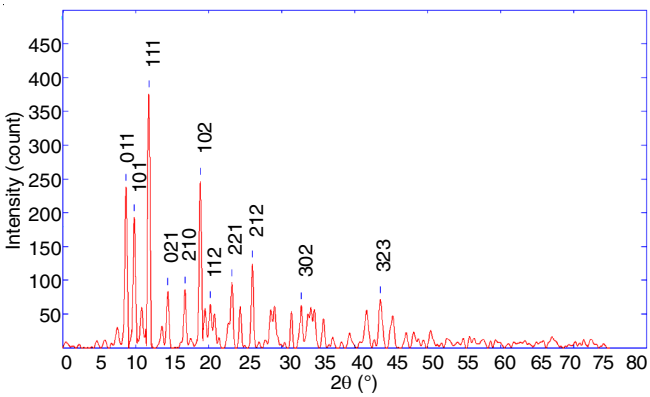

Fig. 1. Powder XRD patterns for iron(II) tartrate nanoparticles

TABLE-1
UNIT CELL PARAMETERS FOR
IRON(II) TARTRATE NANOPARTICLES

Sample	Orthorhombic system unit cell parameters			Angles
	a (Å)	b (Å)	c (Å)	
Iron(II) tartrate nanoparticles	8.76	10.98	8.20	α, β, γ = 90°
Iron(II) tartrate bulk material [8]	8.75	10.98	8.19	α, β, γ = 90°

TABLE-2
CRYSTALLITE SIZE FOR
IRON(II) TARTRATE NANOPARTICLES

Sample name	Average crystallite size (nm)			Strain
	Scherrer's formula	W-H method	TEM	
Iron (II) tartrate nanomaterials	35.28	28.50	30 - 50	0.0032

TEM: TEM images provide direct information of the size, shape, dispersion, structure and morphology of nano-systems. The bright field TEM images of iron(II) tartrate nanoparticles are shown Fig. 2. The majority of the particles sizes in the observed area fall within range of 30 to 50 nm in diameter with the minimum particle size 35.73 nm and the maximum size 49.06 nm in diameter. In the present study, although some nanoparticles are aggregated, the overall distribution suggests the spherical nature of the majority of particles with reasonably small range of diameter variation.

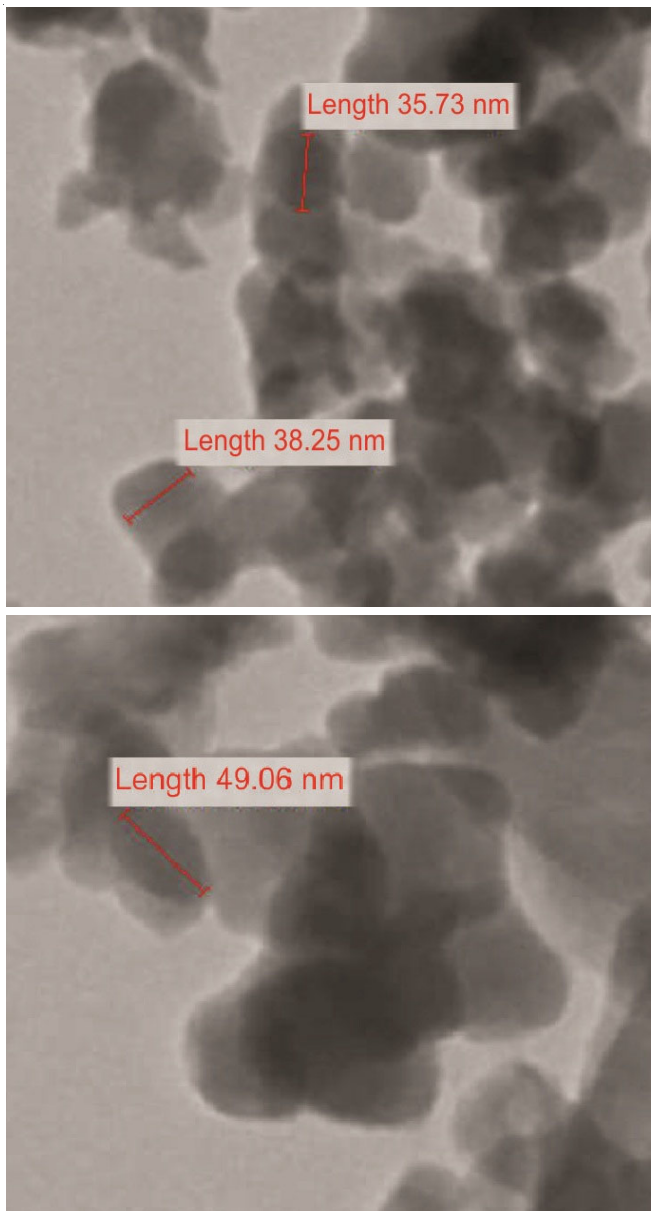

Fig. 2. Bright field TEM images of iron(II) tartrate nanoparticles

FTIR: Fig. 3 shows FTIR spectrum of iron(II) tartrate nanoparticles. The peak observed at 3615.9 cm^{-1} is due to O-H stretching mode indicating the presence of water molecules. The bands around 2937.6, 2859.9 and 2361.4 cm^{-1} are attributed to C-H stretching mode of tartaric acid. The peaks at 1613.6, and 1458.3 cm^{-1} are due to C=O stretching modes of vibrations. The band around 1364.4 cm^{-1} is attributed to λ(C=O) + δ(O-C=O). The peak at 1127.4 cm^{-1} is attributed to δ(C-H) + π(C-H) modes of vibration. The absorption peak at 1057.9 cm^{-1} is attributed to C-O stretching. The peak at 943.5 cm^{-1} is due to stretching modes of carbonyl group ν(C-C). The bands observed around 637.0 cm^{-1} are attributed for CO_2 deformation. Absorption wave numbers below 500 cm^{-1} are assigned for metal-oxygen stretching. Comparing the present FTIR spectrum with reported by Mathivanan *et al*. [13]. It is found that the absorption peak shifts to the higher frequency for O-H stretching mode and the absorption peak shifts to the lower frequency for C-O stretching modes. Comparing FTIR and IR results of earlier work on bulk iron(II) tartrate [6,13], the red and blue shifts in certain absorption peaks observed is due to the nano-structured nature of the sample [10].

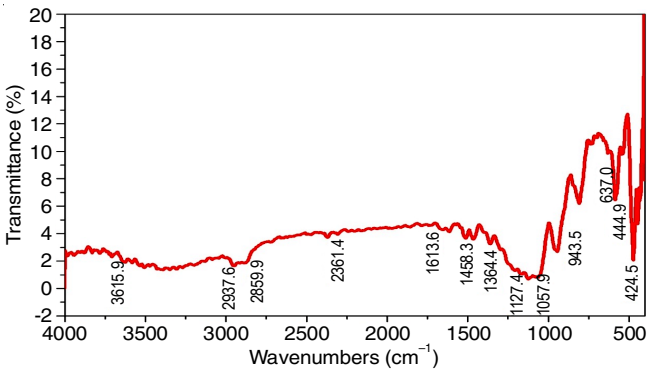

Fig. 3. FTIR spectrum of iron(II) tartrate nanoparticles

Considering a molecular model where the nuclei are represented by point masses and the inter atomic bonds are represented by mass-less springs, which follows Hooke′s law, the force constant can be expressed in N/m as follows [14]:

$$\nu = 1303\sqrt{F\left(\frac{1}{M_1}+\frac{1}{M_2}\right)} \quad (1)$$

where, $1303 = \sqrt{\frac{N_A \times 10^5}{2\pi C}}$, N_A is Avogadro's number (6.0225×10^{23} mol^{-1}) and $C = 3 \times 10^{10}$ cm/s. By considering this simple model, the force constant has been calculated for O-H vibration at 3615.9 cm^{-1}, which is found to be 700 N/m for iron(II) tartrate nanoparticles. On the other hand for the bulk iron(II) tartrate crystals, the force constant is calculated for O-H vibrations occurred at 3510 cm^{-1} [6] which is found to be 660 N/m. The higher value of force constant for nanomaterial is due to the large surface to volume ratio and the large surface energy of nano-particles.

Thermal studies: Thermogravimetric analysis (TGA) and differential thermal analysis (DTA) of iron(II) tartrate nanoparticles were carried out simultaneously in nitrogen atmosphere at a heating rate of 15 ºC/min for a temperature range of 50-800 ºC. Fig. 4 shows the TGA and DTA curves for iron(II) tartrate nanoparticles.

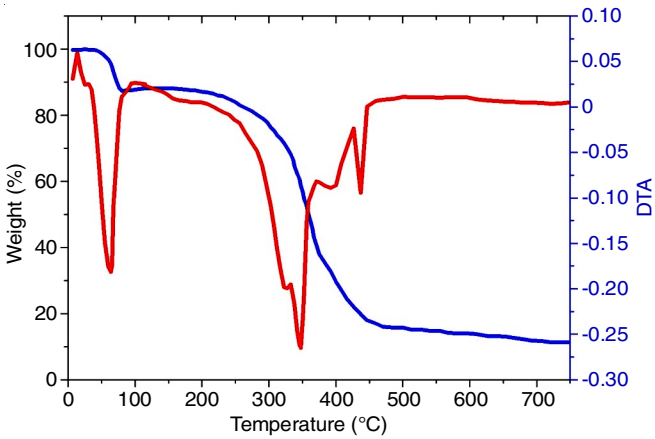

Fig. 4. TG/DTA curve of iron(II) tartrate nanoparticles

It is observed from the plot that iron(II) tartrate nanoparticles remain thermally stable from room temperature to 50 ºC and then start to decompose and completely converted into anhydrous form at 80 ºC .The anhydrous iron(II) tartrate nanoparticles remains stable up to nearly 310 ºC. During the second stage occurring between 310 and 400 ºC, the anhydrous sample is decomposed into oxide form *via* brief metastable stage of iron carbonate at 361ºC. During the second stage of decomposition, the sample loses oxygen, carbon and hydrogen and then converted into ferrous oxide. From DTA plot, the decomposition process occurs through two endothermic reactions at 64 and 347 ºC, respectively. From analysis, two water molecules are found to be associated with iron(II) tartrate nanoparticles. The bulk crystalline iron(II) tartrate remains thermally stable upto 90 ºC and then starts to decompose and becomes completely anhydrous at 150 ºC as reported by Joseph *et al*. [6]. The present nanoparticle samples remain thermally stable up to 50 ºC, which is comparatively less stable due to large surface to volume ratio of the nanoparticles. More number of molecules is on the surface in nanoparticles than the bulk and hence the removal of atoms thermally is easier than bulk form. Table-3 indicates the decomposition processes for iron(II) tartrate nanoparticles with theoretically calculated and experimentally obtained TG results.

TABLE-3
TG-DTA DECOMPOSITION AND PRODUCT FORMED

Sample	Temperature (°C)	Theoretical mass (%) calculated	Experimental mass (%) from plot	Related stage of decomposition
Iron tartrate nanoparticle	Room temperature to 50	100	100	Fe(II) tartrate dihydrate
	80	87.35	87.35	Fe(II) tartrate
	361	49.62	48.06	Metastable state of iron carbonate
	400	29.60	30.72	FeO

Dielectric study: The dielectric constant (ε′) represents the amount of dipole alignment in a given volume along the applied electric field. In present investigation, the measurements were carried out in the frequency range of 10 Hz to 10 MHz within a temperature range from 30 to 100 ºC at the interval of 5 ºC.

Fig. 5 shows the variation of dielectric constant with frequency of applied field at various temperatures. It can be noticed that the dielectric constant decreases as the frequency increases for the temperature range studied. The nanostructured materials have large number of interfaces and also large number of defects present in these interfaces, which is responsible for change in the positive or negative space charge distribution [15]. On applying electric field these space charges move and get trapped by the defects resulting in formation of dipole moment, which is termed as space charge polarization. The interfaces of nanostructured materials have several vacancies equivalent to positive charges giving rise to dipole moments. On application of an external electric field the dipoles rotate and give resultant dipole moment in the direction of applied field, which is known as rotational polarization. The observed decrease in the dielectric constant (ε') with increase in frequency is attributed to the relaxation processes or inability of dipoles to rotate rapidly along with the alternating electric field. Initially, the dielectric constant decreases rapidly with increasing frequency and then slowly decreases at higher frequency. This type of behaviour indicates higher space charge polarizability of the material in the low frequency region [16]. Also as the temperature increases more and more dipole will be oriented resulting in an increased value of dipole moment [17,18]. The dielectric loss (ε'') represents the energy loss occurring during the dipole alignment when the polarity of electric field reverses rapidly and related to the electrical conductivity of materials [19].

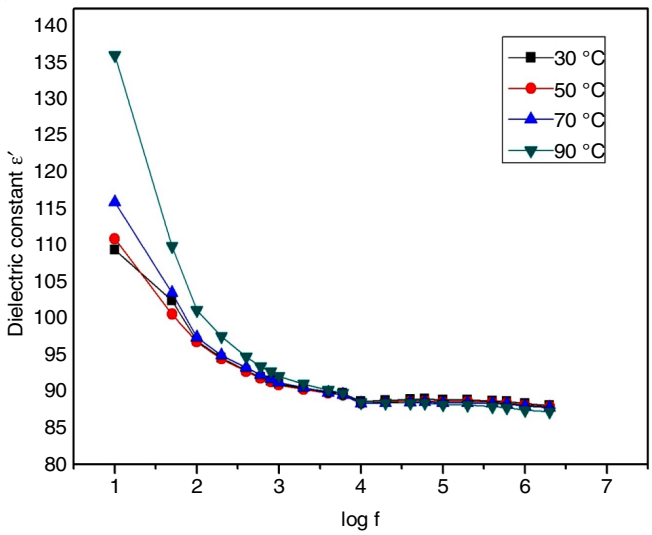

Fig. 5. Variations of dielectric constant at various temperatures with the frequency of applied field for iron(II) tartrate nanoparticles

Variation of dielectric loss (tan δ) with the frequency of applied field at different temperatures is displayed in Fig. 6. The nature of the variation of dielectric loss with frequency is similar to that of dielectric constant with frequency. The value of dielectric loss decreases as the frequency increases.

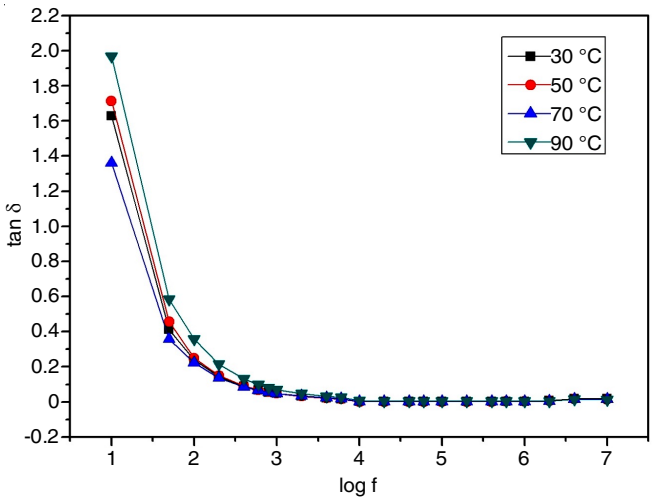

Fig. 6. Dielectric loss versus frequency at various temperatures

The frequency dependence of a. c. conductivity at different temperatures is shown in Fig. 7. The frequency dependence of a.c. conductivity may arise due to free as well as bound carriers. If the conduction is due to free carriers then the conductivity must decrease with increase in frequency [20]. In the present investigation, the a.c. conductivity increases with increasing frequency and therefore, observed a.c. conductivity must be related to bound carriers trapped in the sample.

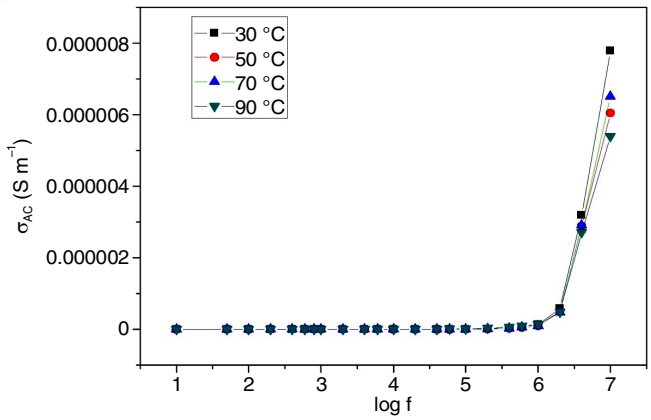

Fig. 7. Variations of a.c. conductivity at various temperatures with the frequency of applied field for iron tartrate nanoparticles

By taking jump relaxation model (JRM) into an account [21] for ionic conduction in solids, there is a high probability for a jumping ion to jump back (unsuccessful hop). However, if the neighbourhood becomes relaxed with respect to the position of ion, then it stays in the new site. The a.c. conductivity gradually increases with the frequency; the conductivity in low frequency region is associated with successful hops, beyond the low frequency region many hops are unsuccessful. This change in ratio of successful to unsuccessful hops result in dispersive conductivity. It can be attributed to the fact that the increment in the frequency enhances the electron hopping frequency [22].

When the conductivity is measured with an AC technique of frequency $\omega = 2\pi f$ the response (known as Jonscher's power law) can be written as follows:

$$\sigma(\omega,T) = \sigma dc\ (T) + A\ (T)\ \omega^{n} \qquad (2)$$

where, σ_{dc} (T) is due to direct current conductivity at $\omega = 0$, A(T) is a factor that depends on temperature but not on ω and n is an exponent in the range of $0 \le n \le 1$ [15,23]. The exponent n behaves in a variety of manners, such as, a constant nature, decreasing with temperature, increasing with temperature, *etc.* [21,24,25]. Vasant [15] compiled the nature of variation of n with temperature for different models of a.c. conduction.

Jonscher's plot (Fig. 8) indicates two distinct regions, *i.e.* nearly horizontal region and the dispersive region. The values of frequency exponent component η obtained from Jonscher's power law are 0.59, 0.55, 0.57 and 0.55 for 30, 50, 70 and 90 ºC, respectively. It has been conjectured from the calculated values of η at various temperatures that correlated barrier hopping (CBH) model mechanism is prevailing. In correlated barrier hopping (CBH) model, the charge carriers hop over the potential barrier between two charged defect states [26,27].

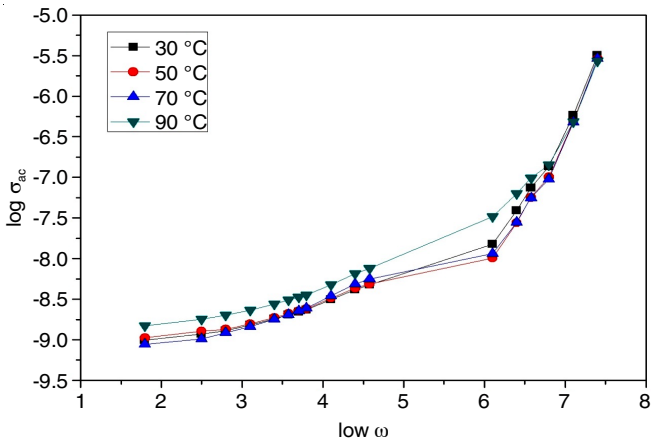

Fig. 8. Jonscher's plot

A better way of displaying the frequency and temperature dependence of a.c. conductivity is to present the a.c. conductivity data in the form of Arrhenius plots at different frequencies [28]. Modifying the Arrhenius equation [22] the conductivity can be expressed as follows:

$$\log \sigma_T = -\frac{E_a \log e}{1000\ K}[1000/T] + \log \sigma_o \qquad (3)$$

where, e = 2.71828182, σ_o is the pre-exponential factor and k is the Boltzmann Constant.

Fig. 9 shows the plot of log (σ_T) *versus* [1000/T] at 1×10^3 Hz. The values of a.c. conduction activation energies obtained from the slope of log (σ_T) *vs.* [1000/T] are given in Table-4. From Table-4, one can notice that as the frequency increases the activation energy for a.c. conduction decreases because the increase in frequency of applied field enhances the charge carriers to jump between localized states.

Vibrating sample magnetometer (VSM) study: According to modern theories the magnetism is inseparable from quantum

TABLE-4
ACTIVATION ENERGY AT VARIOUS TEMPERATURES FOR IRON(II) TARTRATE NANOPARTICLES

a.c. Activation energy (eV) at various frequencies				
1×10^3 Hz	1×10^4 Hz	1×10^5 Hz	1×10^6 Hz	1×10^7 Hz
0.23	0.22	0.11	0.053	0.014

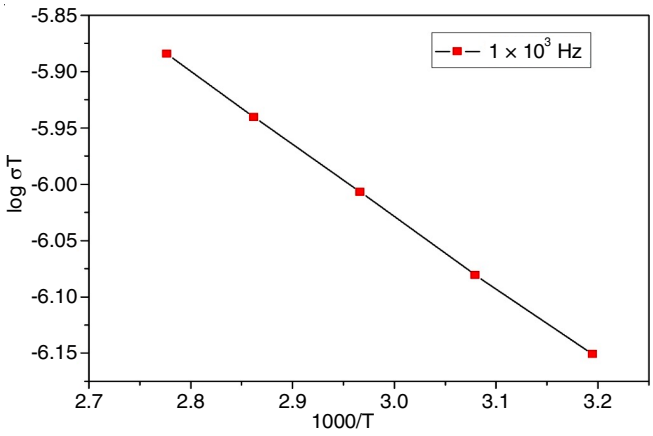

Fig. 9. Plot of log (σ_T) *versus* [1000/T] at 1×10^3 Hz

mechanics. The magnetic moment of a free atom has three principal sources; the spin with which electrons are endowed; their orbital angular momentum about the nucleus; and the change in the orbital moment induced by an applied magnetic field. The first two effects give paramagnetic contributions to the magnetization and the third gives a diamagnetic contribution [29]. In the present investigation for iron(II) tartrate nanoparticles, magnetic field dependent magnetization (M-H) measurements were carried out at different applied magnetic fields from 0.1 Tesla to 1.5 Tesla.

Fig. 10 shows the variation of magnetization with applied magnetic field. It suggests the paramagnetic behaviour. The bulk susceptibility values are calculated at various fields and tabulated in Table-5. Comparing the nature of bulk susceptibility of iron(II) tartrate nanoparticles with already reported values for bulk iron(II) tartrate [30], it is found that iron(II) tartrate nanoparticles exhibit higher values of bulk magnetic susceptibility. This is due to the size effect and large surface to volume ratio of nanoparticles [31]. The bulk susceptibility values for bulk crystalline iron(II) tartrate are reported [30] to be within 8.319×10^{-6} Am^2/kg T to 7.352×10^{-6} Am^2/kg T for magnetic field lying in the range 0.2 T to 1.0 T. The magnetic moment data of bulk crystalline iron(II) tartarate sample are 0.198×10^{-2} to 0.875×10^{-2} range for magnetic field ranging for 0.2 T to 1.0 T as reported earlier [30] in the present case. The

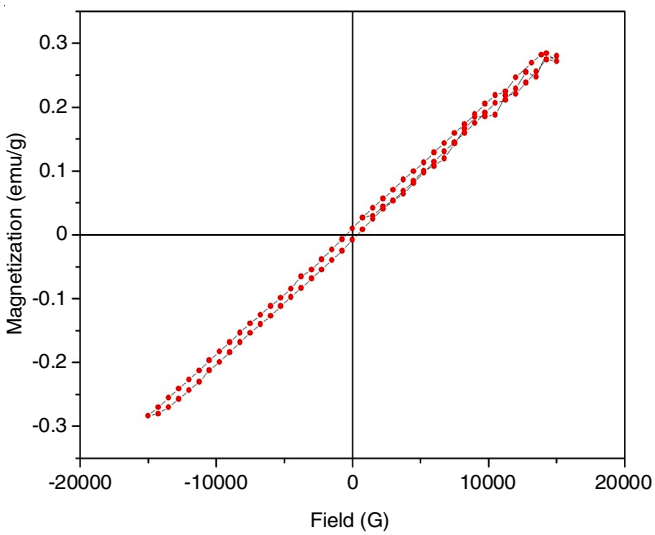

Fig. 10. Variation of magnetization with magnetic field at room temperature

TABLE-5
MAGNETIC MOMENT DATA FOR IRON(II) TARTRATE NANOPARTICLES

Applied magnetic field (Tesla)	Magnetic moment (emu) × 10^{-2}	Bulk susceptibility (Am^2/ kg. T) × 10^{-2}
0.2	0.15	19.74
0.4	0.29	17.96
0.6	0.41	19.05
0.8	0.57	19.33
1.0	0.74	19.63

magnetic moment data varies from 0.15 × 10^{-2} to 0.74 × 10^{-2} for magnetic field 0.2 T to 1.0 T. This suggest that with comparison to bulk crystalline sample, the nanoparticle sample exhibited lower magnetic moment than bulk crystalline sample.

Figs. 11 and 12 show the variation of magnetic moment within the range from 19 to 300 K in the zero field cooled (ZFC) and field cooled (FC) condition, respectively. Both the plots revealed almost identical nature and the magnetic moment is found to be decreasing with increase in temperature. The magnetic moment being inversely proportion to the temperature, *i.e.* M = C/T, the value of magnetic moment decreases as the temperature increases in the paramagnetic substances [29]. Also, there is no remarkable difference in the nature ZFC and FC curves.

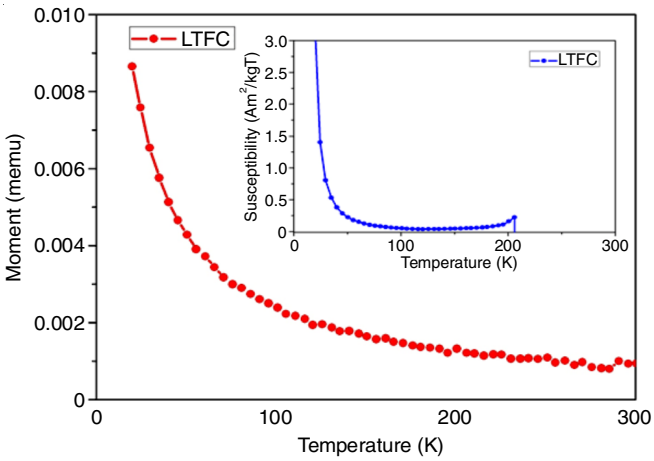

Fig. 11. Variation of magnetic moment at low temperature with zero field cooled, the inset fig shows variation of susceptibility at low temperature

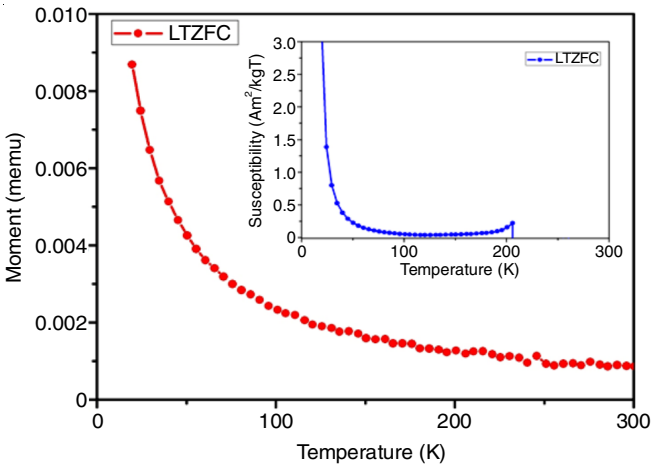

Fig. 12. Variation of magnetic moment at low temperature with field cooled, the inset fig shows the variation of susceptibility at low temperature

Conclusion

Iron(II) tartrate nanoparticles were synthesized by wet chemical method by adopting the surfactant mediated approach. Sodium metasilicate solution facilitated the reaction between tartaric acid and ferrous sulphate without forming any product. The powder XRD study suggested an orthorhombic crystal structure and by employing Scherrer's formula and Williamson & Hall relation, the average crystallite size was found to be 35.28 and 28.50 nm, respectively. The TEM images indicated the spherical morphology and particles size varying from 35 to 49 nm. TG study indicated the thermal stability of iron(II) tartrate nanoparticles upto 50 ºC and at 80 ºC, the sample became anhydrous by giving up two water molecules. The thermal stability is less compared to bulk crystalline samples available in the literature. The dielectric constant and dielectric loss decreased as the frequency increased, for different temperatures. From the variation in the value of exponent n with temperature the correlated barrier hopping (CBH) mechanism was prevailing for a.c. conduction.

ACKNOWLEDGEMENTS

The authors are thankful to Prof. H.H. Joshi, Head, Department of Physics, Saurashtra University, Rajkot, India for his keen interest and UGC for SAP and DST for FIST fundings. One of the authors (UML) is thankful to the administration of SSASIT College, Surat and another author (PMV) is thankful to the Principal, Kamani Science College, Amreli, India for their technical support.

CONFLICT OF INTEREST

The authors declare that there is no conflict of interests regarding the publication of this article.

REFERENCES

1. A.D. Covington, Tanning Chemistry, Cambridge (2009).
2. E.F. George, M.A. Hall and G.J. Deklerk, Plant Propagation by Tissue Culture, Springer (2008).
3. R. Strebel, J. Vasku and H. Selye, *J. Pharm. Pharmacol.*, **14**, 658 (1962); https://doi.org/10.1111/j.2042-7158.1962.tb11156.x.
4. A.C. Clark, D.A. Dias, T.A. Smith, K.P. Ghiggino and G.R. Scollary, *J. Agric. Food Chem.*, **59**, 3575 (2011); https://doi.org/10.1021/jf104897z.
5. P. Grant-Preece, C. Barril, L.M. Schmidtke and A.C. Clark, *J. Agric. Food Chem.*, **65**, 2383 (2017); https://doi.org/10.1021/acs.jafc.6b04669.
6. S. Joseph, H.S. Joshi and M.J. Joshi, *Cryst. Res. Technol.*, **32**, 339 (1997); https://doi.org/10.1002/crat.2170320218.
7. S. Joseph, H.H. Joshi and M.J. Joshi, *Indian J. Pure Appl. Phys.*, **39**, 471 (2001).
8. S.J. Joshi, B.B. Parekh, K.D. Vohra and M.J. Joshi, *Bull. Mater. Sci.*, **29**, 307 (2006); https://doi.org/10.1007/BF02706501.
9. S.J. Joshi, K.P. Tank, B.B. Parekh and M.J. Joshi, *Cryst. Res. Technol.*, **45**, 303 (2010); https://doi.org/10.1002/crat.200900152.
10. U.V. Tarpara, P.M. Vyas and M.J. Joshi, *Int. J. Nanosci.*, **14**, 1550013 (2015); https://doi.org/10.1142/S0219581X15500131.
11. P.D. Solanki, S.R. Vasant and M.J. Joshi, *Int. J. Appl. Ceram. Technol.*, **11**, 663 (2014); https://doi.org/10.1111/ijac.12227.
12. L. Kumar, P. Kumar, A. Narayan and M. Kar, *Int. Nano Lett.*, **3**, 8 (2013); https://doi.org/10.1186/2228-5326-3-8.

13. V. Mathivanan and M. Haris, *PRAMANA-J. Phys.*, **81**, 177 (2013); https://doi.org/10.1007/s12043-013-0564-x.
14. K.P. Tank, Ph.D. Thesis, Department of Physics, Saurashtra University, Rajkot, India (2013).
15. S.R. Vasant, Ph.D. Thesis, Department of Physics, Saurashtra University, Rajkot, India (2015).
16. F.M. Reicha, M. El-Hiti, A.Z. El-Sonbati and M.A. Diab, *J. Phys. D Appl. Phys.*, **24**, 369 (1991); https://doi.org/10.1088/0022-3727/24/3/020.
17. K. Somashekhara Udupa, P. Mohan Rao, S. Aithal, A.P. Bhat and D.K. Avasthi, *Bull. Mater. Sci.*, **20**, 1069 (1997); https://doi.org/10.1007/BF02745057.
18. M. Shakir, B.K. Singh, R.K. Gaur, B. Kumar, G. Bhagavannarayana and M.A. Wahab, *Chalcog. Lett.*, **6**, 655 (2009).
19. M. Ravi, S. Song, K. Gu, J. Tang and Z. Zhang, *Mater. Sci. Eng. B*, **195**, 74 (2015); https://doi.org/10.1016/j.mseb.2015.02.003.
20. M.N. Kamalasanan, N.D. Kumar and S. Chandra, *J. Appl. Phys.*, **74**, 5679 (1993); https://doi.org/10.1063/1.354183.
21. K. Funke, *Prog. Solid State Chem.*, **22**, 111 (1993); https://doi.org/10.1016/0079-6786(93)90002-9.
22. A.K. Roy, K. Prasad and A. Prasad, *ISRN Ceram.*, **Article ID 369670** (2013); https://doi.org/10.1155/2013/369670.
23. J.O. Lopez and R.G. Aguilar, *Rev. Mex. Fis.*, **49**, 529 (2003).
24. S.R. Elliott, *Adv. Phys.*, **36**, 135 (1987); https://doi.org/10.1080/00018738700101971.
25. S. Upadhyay, A.K. Sahu, D. Kumar and O. Parkash, *J. Appl. Phys.*, **84**, 828 (1998); https://doi.org/10.1063/1.368143.
26. S.R. Elliott, *Philos. Mag.*, **36**, 1291 (1977); https://doi.org/10.1080/14786437708238517.
27. G.E. Pike, *Phys. Rev. B*, **6**, 1572 (1972); https://doi.org/10.1103/PhysRevB.6.1572.
28. H. Mahamoud, B. Louati, F. Hlel and K. Guidara, *Bull. Mater. Sci.*, **34**, 1069 (2011); https://doi.org/10.1007/s12034-011-0163-8.
29. C. Kittel, Introduction to Solid State Physics, Wiley Eastern: New Delhi, edn 7 (2007).
30. S. Joseph, H.H. Joshi, M.J. Joshi, N.V. Patel and M. Sarcar, *Indian J. Phys*., **71A**, 643 (1997).
31. I. Bashar, I.M. Obaidat, B.A. Albiss and Y. Haik, *Int. J. Mol. Sci*., **14**, 21266 (2013); https://doi.org/10.3390/ijms141121266.